TUDelft

Delft University of Technology

The effect of Nb on the hydrogen embrittlement susceptibility of Q&P steel under static and dynamic loading

Vercruysse, Florian; Claeys, Lisa; Depover, Tom; Verleysen, Patricia; Petrov, Roumen H.; Verbeken, Kim

Important note
To cite this publication, please use the final published version (if applicable).
Please check the document version above.

The effect of Nb on the hydrogen embrittlement susceptibility of Q&P steel under static and dynamic loading

Florian Vercruysse [a], Lisa Claeys [b], Tom Depover [b,*], Patricia Verleysen [a], Roumen H. Petrov [a,c], Kim Verbeken [b,*]

[a] *Department of Electromechanical, Systems & Metal Engineering, Research Group Materials Science and Technology, Ghent University, Tech Lane Science Park Campus A 46, 9052, Zwijnaarde, Belgium*
[b] *Department of Materials, Textiles and Chemical Engineering, Research Group Sustainable Materials Science, Ghent University, Tech Lane Science Park Campus A 46, 9052, Zwijnaarde, Belgium*
[c] *Department of Materials Science and Engineering, Delft University of Technology, Mekelweg 2, 2628CD, Delft, the Netherlands*

ARTICLE INFO

ABSTRACT

In the present study, the effect of Niobium (Nb) on the hydrogen embrittlement resistance of Quenched and Partitioning (Q&P) steel is investigated. For this purpose, the hydrogen uptake level and its impact on the mechanical properties of a Nb-free and a 0.024 wt% Nb Q&P steel are thoroughly analysed. The hydrogen trapping capacity is evaluated via thermal desorption spectroscopy (TDS). In-depth analysis of the desorption kinetics at different heating rates allows identification and quantification of the available trapping sites. The hydrogen embrittlement sensitivity of both steels is characterized using static and dynamic tensile tests. The addition of Nb results in an increase of the hydrogen concentration by more than 25%. The larger hydrogen content in the Nb steel, as a result of the higher fraction of grain boundaries/interphases, gives rise to a more severe embrittlement of the Nb steel compared to the Nb-free one. In addition to the larger hydrogen fraction in the Nb Q&P steel, the larger retained austenite fraction of low stability is detrimental due to the larger fraction of high carbon martensite formed when straining. This results in higher susceptibility to hydrogen embrittlement of the Nb microalloyed steel due to the brittle character of the high carbon martensite that forms easily during straining. Under dynamic loading conditions, the hydrogen embrittlement of both steels is minimal, which is attributed to a reduced hydrogen diffusion and the suppression of the transformation induced plasticity (TRIP) effect due to adiabatic heating.

1. Introduction

The development of advanced high strength steels (AHSS) for the automotive industry has received constant attention over the past few decades because of increasingly stringent regulations related to fuel consumption, CO_2-emissions and passenger safety. Currently, the third generation of AHSS is being developed. This generation aims to achieve mechanical properties between those of the first and second generation, though without the use of expensive alloying elements as was the case in the 2nd generation [1,2]. One of the most promising 3rd generation AHSS are Quenching and Partitioning steels (Q&P).

Q&P steels were first reported by Speer et al., in 2003 and have gradually received more attention [3]. The microstructure consisting of tempered martensite and 10–15% retained austenite (RA) results in an excellent combination of strength and ductility [4–6]. The RA transforms to martensite under (plastic) straining, locally strengthening the material and as such postponing necking leading to a high uniform elongation, i.e. the so-called Transformation induced plasticity (TRIP) effect [7]. The thermal cycle resulting in the Q&P microstructure is based on an incomplete quenching to a temperature situated in between the martensite start (M_s) and martensite finish temperature (M_f). The fraction of martensite formed, typically between 80 and 90%, is selected to release sufficient carbon to stabilize the RA in the subsequent partitioning step [3,6]. In the partitioning step, the steel is heated up to a temperature above M_s and held at this temperature. By doing so, the carbon diffuses from the supersaturated martensite to the neighbouring

---

untransformed austenite. The carbon enrichment of austenite lowers the M_s temperature and, as such, effectively stabilises austenite ensuring that it will not transform when further quenched to room temperature. In some cases, when the carbon content of the untransformed austenite is not sufficiently high to stabilize the austenite, fresh martensite could form during the final cooling after partitioning. This fresh martensite is considered undesirable because it is hard, brittle and may lead to a general embrittlement of the steel [8].

Hydrogen embrittlement (HE) is considered a critical issue for the application of AHSS in several industrial fields since it might give rise to a premature and unpredictable failure [9–11]. Multiple authors have found that the HE susceptibility increases with the steel strength level [10,12]. In Q&P steels, additionally, the solubility of hydrogen in austenite is significantly larger compared to martensite [13,14]. The high solubility of hydrogen in austenite is found to be problematic when martensite transformation occurs upon straining [15]. Some authors report austenite to be beneficial as it acts as an effective hydrogen trapping site due to the high solubility and low diffusivity of hydrogen in austenite, whereas others consider the fresh martensite formed during the transformation of RA to be highly susceptible to HE [14,16]. The latter was attributed to the combination of the local high internal stresses caused by the volume expansion associated with the martensite formation, the non-uniform hydrogen distribution and the high number of pinned dislocations [13,17–19]. The non-uniform hydrogen distribution is a result of a higher hydrogen solubility phase transforming into a lower solubility phase, leading to supersaturation of the freshly formed martensite upon straining. These three factors result in hydrogen-assisted crack (HAC) initiation to occur at the M/A interphase [13]. Many studies confirm that the austenite stability could determine whether retained austenite is beneficial or not when hydrogen is introduced in the metal microstructure [20–22].

Grain refinement is known to be an effective strategy to improve both strength and toughness of steels. Next to the refinement of grains via thermo-mechanical processing, also the addition of micro-alloying elements has been extensively used. The addition of Nb results in the formation of Nb carbides (NbC). The Nb carbides (NbC) not only give rise to grain refinement and precipitation hardening, though also might affect the hydrogen embrittlement susceptibility. Indeed, carbides or other precipitates can act as beneficial hydrogen traps [21,23–26]. The binding energy of the traps is crucial in the effect it has on the HE sensitivity. Finely distributed deep, irreversible traps can act as effective hydrogen storage sites, lowering the amount of diffusible hydrogen, which is considered to be the main cause of the observed ductility loss. Traps characterised by a low binding energy (reversible trapping sites), on the other hand, can still release hydrogen for diffusion and, thus, act as hydrogen sources during straining. The energy of NbC trapping sites is reported to be between 20 (weak) and 80 (deep) kJ/mol depending on its size, coherency with the matrix and location of actual trapping, e.g., at the interface or inside the carbide [23,27].

Q&P steels have potential to be used as structural components of cars. For these applications, their behaviour at high strain rates that occur during crashes is important. Previous studies of the authors showed that at dynamic strain rates, the TRIP effect, and therefore the behaviour of Q&P steels, is significantly affected. This was mainly attributed to the influence of adiabatic heating on the austenite stability [28]. Since the transformation of austenite plays an important role in HE, an increased strain rate might affect the HE. Additionally, the reduced diffusion at dynamic rates might also play a role, as shown for a DP steel [29].

Although some research has been carried out on the effect of the stability of austenite on the hydrogen susceptibility, little is known on the coupled effect of austenite stability, grain refinement and adiabatic heating during high strain rate testing [20]. Therefore, the present study focuses on the effect of the addition of Nb on the HE susceptibility of a Q&P steel under static and dynamic loading conditions. To relate the mechanical properties with the microstructure of the studied steels,

features such as the grain size, and the fraction and stability of the RA phase will be determined. Additionally, the hydrogen desorption and trapping sites will be quantified via thermal desorption spectroscopy.

2. Materials

The chemical composition of the two steels, i.e. a Nb free and a Nb micro-alloyed steel, studied in this work is shown in Table 1. The data in the table are based on a chemical analysis of the steels after casting.

The steels were cast, hot rolled and subsequently cold rolled with a total cold rolling reduction of 50% into sheets with a final thickness of 1.5 mm. More details can be found in Ref. [30]. The Q&P cycle was designed based on dilatometer experiments with the aim to minimise the fraction of fresh martensite as this is generally accepted to be detrimental for the ductility of Q&P steels [8]. Samples were heated in a Vatron MULTIPAS annealing simulator to 870 °C and soaked for 100 s to homogenise the chemical composition of the austenite. Subsequently, the Nb and Nb free steel were quenched to 290 °C and 300 °C, respectively. The difference in quenching temperature resulted from the reduction of the M_s temperature by the Nb/Cr addition [31,32]. Apart from the reduction in the M_s temperature, the effect of the Cr addition is negligible regarding the hereafter discussed results in comparison to the Nb addition and will therefore not be further mentioned in the following sections [33]. At the selected temperatures, the steels contain, according to calculations based on the Koistinen-Marburger (KM) model, 11% and 14% untransformed austenite, respectively [31]. A partitioning temperature of 400 °C and duration of 50 s was chosen. After quenching, the fractions of the fresh martensite in the final microstructures were observed to be very small (<2%). The temperature of the process was controlled by a K1-type thermocouple and resulted in a homogenously heat-treated area of $100 \times 200 \times 1.5$ mm^3 from which the samples needed for mechanical testing as well as for microstructural analyses were machined.

3. Experimental techniques

3.1. Microstructural observation

Scanning electron microscopy (SEM) was used to characterise the fracture surface of the steels after tensile testing. The images were obtained via a Quanta 450 FEG-SEM operated at 20 kV with a beam current of ~2.2 nA. Electron backscattered diffraction (EBSD) measurements were recorded on the same SEM with the sample tilted at 70°, on a working distance of 16 mm and a step size of 50 nm in a hexagonal scan grid.

The orientation data were post-processed by means of Ametek EDAX-TSL-OIM Data analysis v7.3 after applying the "*grain confidence index standardisation*" and "*grain dilation*" clean-up procedures to the original orientation data. Grains were defined as regions of the scan that contain a minimum of 5 neighbouring points with misorientation between two points of less than 5°. The derivation of grain size and phase fraction of the three main structural constituents present in the Q&P steel (retained austenite, fresh and tempered martensite) was based on EBSD data as well. Grain average image quality (GAIQ) was used to distinguish between tempered and fresh martensite as the latter has a low GAIQ [34]. All data points with a size larger than 5 pixels not being part of a grain boundary, containing multiple rows and low GAIQ value were attributed to fresh martensite [35].

As there were detection limits inherently present in the EBSD mea-

Table 1
Chemical composition of the Q&P steels (wt%).

	C	Si	Mn	Al	Cr	Nb	Fe
Nb free steel	0.199	1.260	2.350	0.018	0.025	–	Bal.
Nb steel	0.192	1.260	2.410	0.019	0.300	0.024	Bal.

surements, the total fraction of retained austenite was determined by XRD measurement using a Siemens Kristalloflex D5000 diffractometer operating with a Mo-K$_\alpha$ source at 40 kV and 40 mA. All scans were performed with a step size of 0.03° and 20s dwell time. The retained austenite fraction was determined based on the {200}α, {211}α, {220}γ and {311}γ diffraction peaks after subtracting the Kα$_2$ and the background radiation from the raw data [36]. The austenite lattice parameter is determined from the extrapolation of the austenite peaks when plotted against the $\cos^2(\theta)/\sin(\theta)$ [37,38]. From the lattice parameter (a_γ), the carbon fraction (x_C) was derived using the following formula based on the Mn fraction (x_{Mn}) of the general steel composition [37,38]. Mn diffusion is prohibited under the para-equilibrium conditions met during partitioning.

$$a_\gamma = 0.3556 + 0.00453x_C + 0.000095x_{Mn} \tag{1}$$

Finally, transmission electron microscopy (TEM) was used to characterise the NbC precipitates. A JEOL 2200FS HRTEM was used, operated with an accelerating voltage of 200 kV. Energy-dispersive X-ray (EDX) spectroscopy was used to confirm the chemical composition of the observed precipitates.

3.2. Hydrogen charging and characterisation

Atomic hydrogen was introduced in the specimens by electrochemical charging in a 0.5 M sulphuric acid (H$_2$SO$_4$) electrolyte in which 1 g/l thiourea (CH$_4$N$_2$S) was added. The addition of thiourea reduces the recombination to molecular hydrogen gas by hydrogen atoms adsorbed at the steel surface. Hydrogen charging occurred in an electrochemical cell in which the sample acted as the cathode positioned in between two platinum counter anodes. The samples, which were disk-shaped with a diameter of 20 mm and a thickness of 1.5 ± 0.01 mm, were charged galvanostatically for 4 h at a constant current density of 0.8 mA/cm^2.

Thermal desorption spectroscopy (TDS) was used to stud the hydrogen desorption kinetics in the materials as well as to evaluate the hydrogen concentration within each steel. The hydrogen desorption kinetics can be used to determine the hydrogen traps present in the material as well as to provide information on the trap density and their corresponding desorption activation energy. The hydrogen charged disks were heated at specific heating rates, i.e. 600 °C/h, 900 °C/h and 1200 °C/h. Hydrogen will desorb from the samples when the temperature is sufficiently high to overcome the desorption activation energy of the traps. The hydrogen signal was measured by a mass spectrometer. This resulted in a flux of hydrogen leaving the sample as a function of temperature. From the peak maximum positions for every heating rate, the desorption activation energy of the trapping site can be derived via the Kissinger equation [39]:

$$\frac{d(\ln \frac{\Phi}{T_{max}^2})}{d(\frac{1}{T_{max}})} = -\frac{E_a}{R} \tag{2}$$

where Φ is the heating rate (K/min), T_{max} (K) the TDS peak temperature, R (J/(K mol)) the universal gas constant and E_a (J/mol) the detrapping activation energy for the specific hydrogen trapping site associated with T_{max}. Deconvolution of the spectrum allows to determine traps of different activation energy as well as their relative fraction. The deconvoluted peaks are fitted to the experimental curve by varying their amplitude, full width at half maximum and peak maximum position.

3.3. Mechanical characterisation

To characterise the quasi-static mechanical properties, a conventional Instron™ 5569 tensile test device equipped with a 50 kN load cell was used. The tensile tests were performed at nominal strain rates ranging from 0.001 s^{-1} to 0.3 s^{-1}.

Split Hopkinson Tensile Bar (SHTB) experiments were performed to characterise the mechanical properties under dynamic loads [40].

During the SHTB tests, the samples were fixed between two long bars and loaded by a mechanical tensile wave. The amplitude of the tensile wave can be adjusted, which allows controlling the strain rate in the sample. For all dynamic experiments, a strain rate of approximately 500 s^{-1} was aimed at. SHTB tests require the use of samples with reduced dimensions [41]. Therefore, sub-sized tensile samples with the dog-bone geometry and dimensions as presented in Fig. 1 were used. This reference geometry is characterised by a transition from the clamping region to the gauge section with a radius of 1 mm, denoted as R1 geometry. The samples were fixed to the test bench with pins. The samples were extracted along the rolling direction of the cold rolled sheet.

To eliminate the influence of sample geometry and boundary conditions, identical samples and pins to hold the samples were used for the static tests. As such, all differences observed between the static and dynamic test results can be attributed to the strain rate sensitivity of the material [41].

The duration of dynamic tests is so short that the heat generated by plastic deformation of the specimen cannot be dissipated to the environment. The adiabatic temperature increase of the sample is calculated assuming that a fraction β of the plastic work, i.e. the Taylor-Quinney coefficient, is converted into heat. For steels, generally, a β value of 0.9 is adopted. However, as the transformation of austenite to martensite is exothermal, in present study, a coefficient equal to 1 is used to, at least partially, account for this [42].

For each test condition, three experiments were conducted. The reported engineering strain to failure (FS) values are average values for the three tests, while the presented stress-strain curves are representative curves.

All tensile tests were carried out ex-situ. The hydrogen charged tensile tests, irrespective of the strain rate applied, were conducted at a fixed time of 4 min after the samples were taken from the hydrogen charging set up. The embrittlement index (EI) used to evaluate the effect of hydrogen on the ductility of the material is derived as follows:

$$EI = \frac{\varepsilon_f^{Air} - \varepsilon_f^{H}}{\varepsilon_f^{Air}} \tag{3}$$

where ε_f^{Air} and ε_f^{H} are resp. the engineering strain at fracture for the reference samples tested in air and the H-charged samples.

4. Results

4.1. Microstructural observations

The addition of Nb changed the microstructure of the investigated Q&P steel. EBSD measurements indicated that Nb resulted in a refinement of the tempered martensite. Fig. 2 shows an example of the performed EBSD measurements for the Nb added steel. The average grain diameter in the Nb free steel is 3.7 μm while the Nb-steel is characterised by an average martensite diameter of 2.7 μm (Table 2). Next to the refinement of the martensite grains, a smaller prior austenite grain size was observed as well. Analysing the prior austenite grains via the ARPGE reconstruction software, showed that Nb resulted in a refinement of the grains by 30% [43]. However, when determining the RA grain size by EBSD, no refinement caused by the Nb addition was observed.

Next to the analysis of the grain size, EBSD measurements are used to evaluate the fractions of the phases present in the Q&P steel. It is observed that the addition of Nb resulted in a minor increase in the fraction of fresh martensite (2% compared to 1%). This fresh martensite fraction is crucial as these grains could be damage initiation points, as discussed above.

A TEM-EDS analysis is performed to evaluate the type of retained austenite and the presence of carbides in the Nb added steel. It is observed that the RA s present in two distinct morphologies; blocky as well as film-type retained austenite. The latter type shows a thickness between 10 and 100 nm. The differences between the Nb comprising and
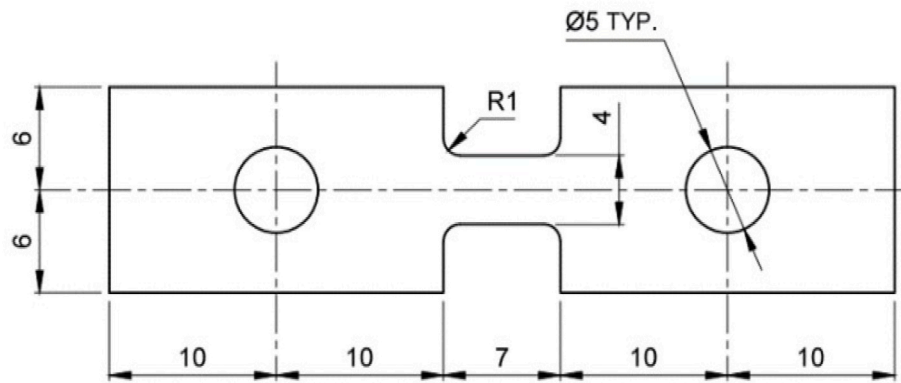
Fig. 1. Representation of the dog-bone geometry used for both the quasi-static and dynamic tensile tests (in mm).
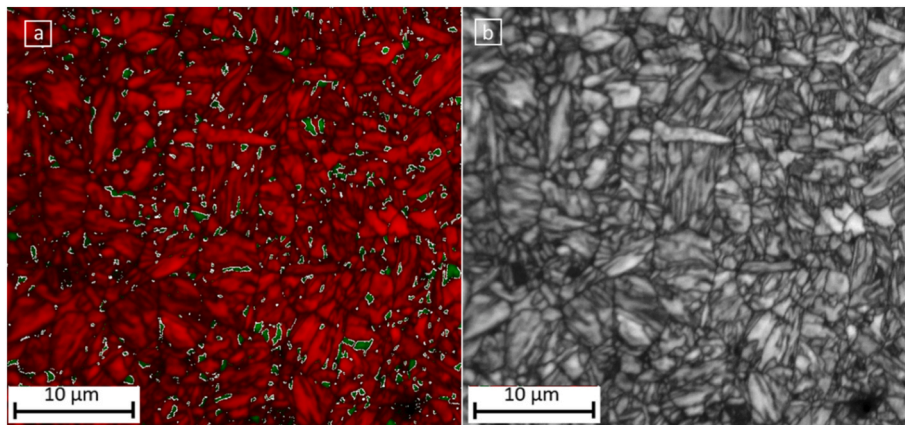

Fig. 2. EBSD images of the Nb added steel. (a) phase map with martensite in red and austenite in green. (b) image quality (IQ) map of which low IQ zone are an indication of fresh martensite..

Table 2
Calculated grain average diameter (μm) based on EBSD measurements [44].

	Prior austenite	Martensite	Retained austenite
Nb free steel	8.03 ± 0.80	3.70 ± 0.25	0.46 ± 0.04
Nb steel	6.11 ± 0.90	2.69 ± 0.28	0.52 ± 0.05

Nb free steel were minimal under these TEM observations. The main differences observed between both types of steel is the presence of NbC in the Nb-comprising steel (cf. Fig. 3). Precipitates in the order of 5–20 nm are observed [44].

Due to the small size of the film-type retained austenite grains, it was opted to use X-ray diffraction analysis in order to determine the total volume fraction of retained austenite. The XRD results indicated the fraction of RA to be larger for the Nb comprising steel. With the XRD analysis, even the smallest RA grains were detected. The Nb comprising steel was characterised by a RA fraction of 13% while the Nb free steel had a RA fraction of 10.4% which is in agreement with the calculated austenite fraction based on the KM-model (Table 3). It is noticed that while half of the RA grains are detectable by EBSD in the case of the Nb free steel only 35–40% are detected in the Nb comprising steel. This suggests that the RA grain size of the Nb steel is on average smaller than in the Nb free steel. XRD analysis was also used in order to evaluate the carbon content in austenite by the peak position being related to interstitial carbon atoms. It was observed that the larger RA fraction of the Nb-comprising steel had a lower carbon content when compared to the smaller fraction in the Nb free steel, i.e., 1.06 wt% and 1.14 wt%, respectively.

4.2. Hydrogen charging and characterisation

The fraction of hydrogen, derived via TDS measurements, in the Nb and the Nb free Q&P steel is 5.09 ± 0.38 and 4.12 ± 0.18 wppm, respectively (Table 4). Hence, the hydrogen content was about 25% larger in the Nb steel compared to the Nb free steel. The results of the TDS experiments are presented in Fig. 4. To derive the activation energy of the hydrogen trapping sites and to link them with the microstructure of both steels, TDS measurements at different heating rates were used. A desorption peak situated from room temperature up to 300–350 °C is observed. Next to the larger fraction of hydrogen in the Nb steel compared to the Nb free steel, peak shift to higher temperatures is observed. The peak maximum in the Nb steel is shifted about 50 °C higher than the one of the Nb free steel.

The observed TDS peak was, for each heating rate and alloy, deconvoluted into 2 peaks in order to derive, based on the Kissinger equation, the desorption activation energy of the corresponding trapping site (Fig. 5). Similar to the cumulative peak, a shift to elevated temperatures is observed for the deconvoluted peaks of the Nb steel. However, most noteworthy is the increase in the height of the peaks when comparing the Nb and the Nb free steel. While the height increase for the first peak is minimal, an increase in the 2nd peak of more than 40% is observed when comparing the Nb free and Nb Q&P steel. This is further quantified by the integration of the peaks, as shown in Fig. 6-a. The activation energies that correspond to both peaks are shown in Table 5. Although the values for both steels are similar, the Nb steel is characterized by activation energies which are 1.5–2 kJ/mol higher than those in the Nb free steel. The grain boundary analysis that was carried out by EBSD showing the total density of low and high angle
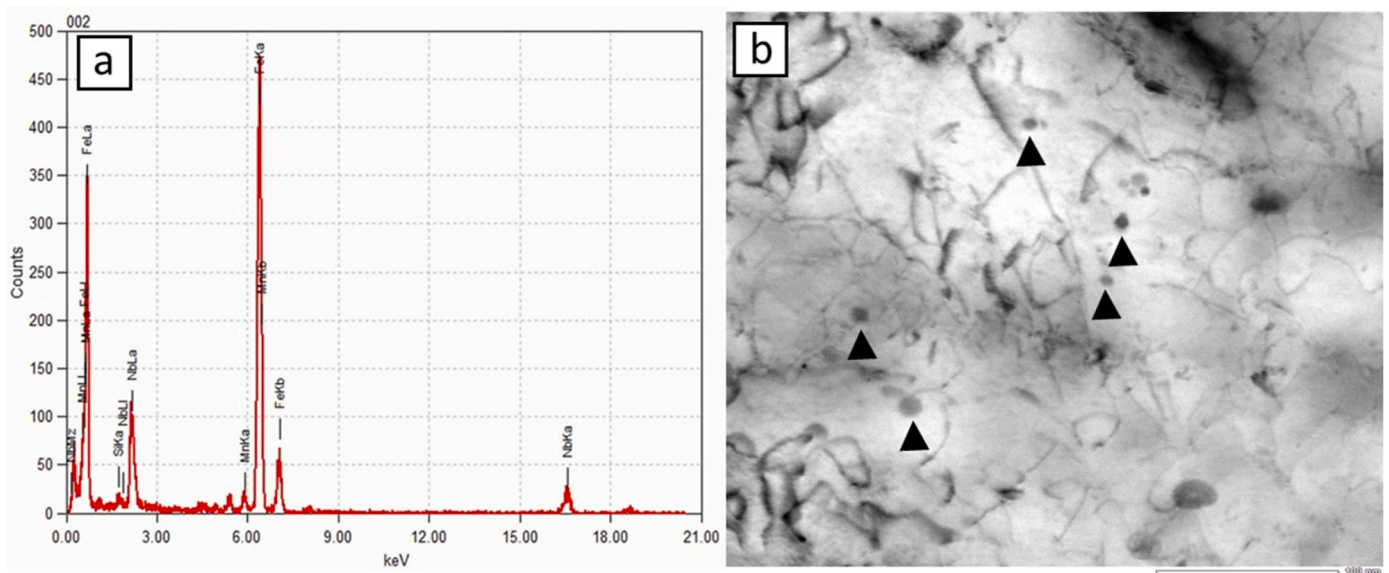
Fig. 3. (a) EDX and (b) TEM image of Nb precipitates. The precipiates are indicated with black triangles.

Table 3
Quantification of the Tempered Martensite (TM), Fresh Martensite (FM) and retained austenite (RA) fractions based both on EBSD and XRD data as well as the average carbon content of retained austenite and martensite based on the XRD analysis [44].

	TM (%)	FM (%)	RA EBSD (%)	RA XRD (%)	C content RA (wt.%)	C content martensite (wt.%)
Nb free steel	88.6 ± 0.5	1.0 ± 0.5	5.4 ± 0.02	10.4 ± 0.9	1.14 ± 0.03	0.09 ± 0.03
Nb steel	85.0 ± 0.5	2.0 ± 0.5	4.9 ± 0.3	13.0 ± 1.1	1.06 ± 0.03	0.07 ± 0.03

Table 4
Hydrogen fraction measured in the Nb free and Nb steel after charging derived from TDS measurements.

	Nb free steel	Nb steel
Hydrogen fraction (wppm)	4.12 ± 0.18	5.09 ± 0.38

grain boundaries, characterised by a misorientation of 5–15° and 15–62.8°, respectively, is presented in Fig. 6-b.

4.3. Mechanical properties

4.3.1. Static tensile properties

The static tensile properties of uncharged and hydrogen charged samples were evaluated at a 0.3 s^{-1} strain rate. Hydrogen charged samples were also tested at a 300 times lower strain rate, i.e., at 0.001 s^{-1}. The obtained tensile curves for the Nb free and Nb steel are presented in Fig. 7-a and 7-b, respectively. For both steels, a clear difference is observed between the charged and reference air tested samples. At the two strain rates, a significant reduction in ductility is observed in the hydrogen charged samples. At the lowest strain rate, the embrittlement is most severe. Indeed, the plastic deformation has almost completely disappeared. For samples tested at 0.3 s^{-1}, the fracture occurred in the centre of the gauge section, while the samples tested at 0.001 s^{-1} fractured within the transition zone from the clamping region to the gauge section. However, comparing the Nb and Nb free 0.001 s^{-1} curves, a slightly higher value of plastic strain is reached in the Nb steel. This observation was confirmed by post-mortem observation of thinning of the shoulder section of the Nb samples which was absent for the Nb free samples.

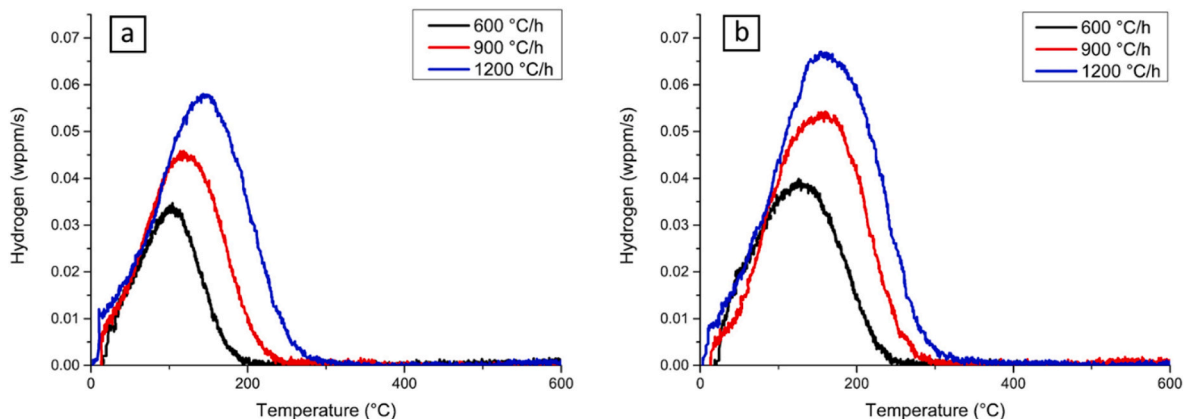At the highest static strain rate of 0.3 s^{-1}, on the contrary, the

Fig. 4. TDS measurements of (a) the Nb free and (b) the Nb steel derived under a heating rate of 600 °C/h, 900 °C/h and 1200 °C/h.
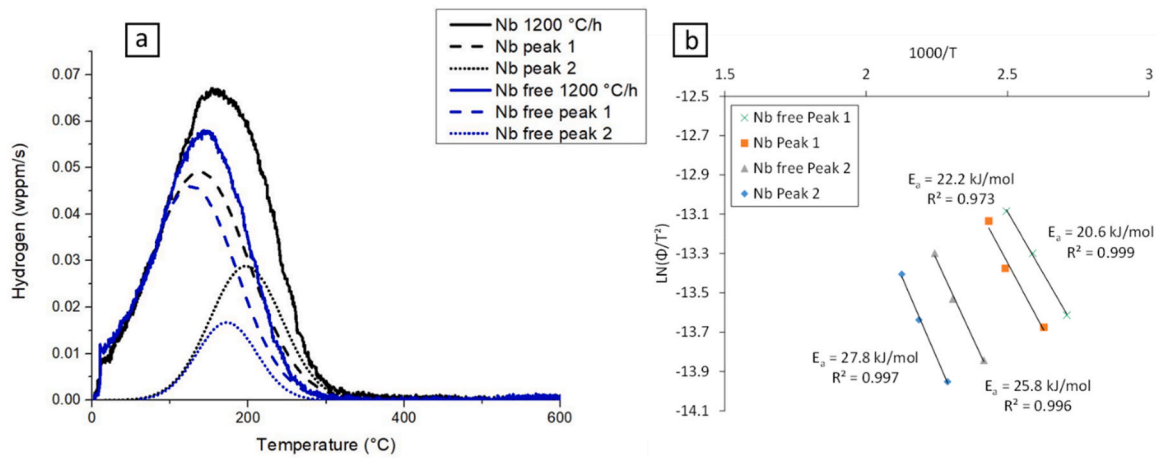
Fig. 5. (a) Deconvolution of the TDS peak into two peaks for the Nb free and Nb steel. (b) Kissinger plot of the four fitted peaks.
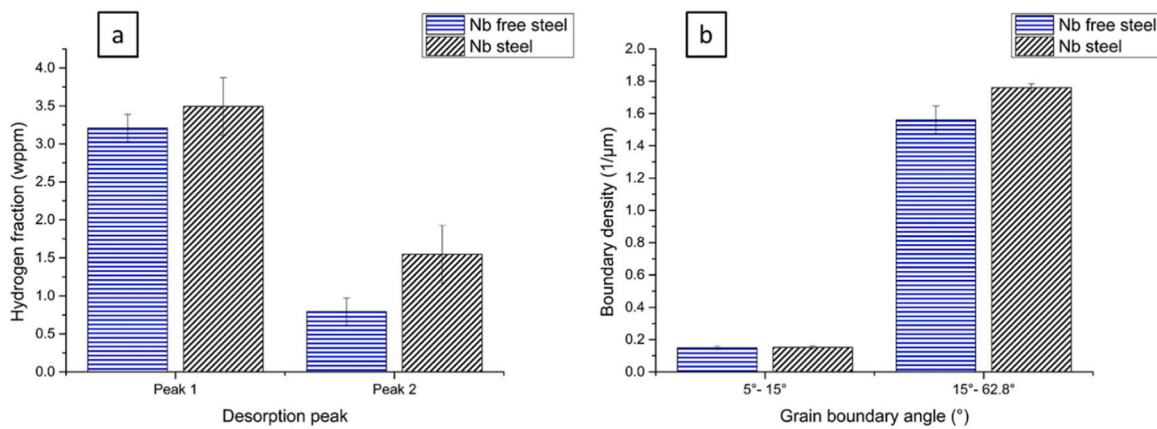

Fig. 6. Quantification of (a) the deconvoluted TDS data into 2 peaks with an activation energy as presented in Table 5 and (b) low and high grain boundary density for both steels.

Table 5
Desorption activation energy (kJ/mol) corresponding to the deconvoluted TDS peaks of the Nb free and Nb steel.

Activation energy (kJ/mol)	Peak 1	Peak 2
Nb free steel	20.6	25.8
Nb steel	22.2	27.8

decrease in ductility is more severe in the Nb samples. For the Nb steel, an embrittlement index of 52.0% is observed, while the Nb free steel has an EI of 40.2%. High speed camera imaging was used to capture the fracture of the samples. For all samples tested at 0.3 s^{-1}, the transverse fracture initiated in the centre and propagated to the edges. Although in uncharged conditions the sample failed as expected and with similar elongation (not presented), samples tested at the lowest static strain rate fractured outside the gauge zone. Therefor no meaningful EI could be derived at 0.001 s^{-1}. As a result, to obtain a second testing condition at low strain rates, an adapted sample geometry is proposed, as elaborated in the next section.

4.3.2. Static properties with adapted geometry

The hydrogen charging of the steels considered in this study reduced their plastic deformation capacity to such an extent that tensile testing at a strain rate of 0.001 s^{-1} using the geometry presented in Fig. 1 resulted in fracture outside the gauge section. To obtain reliable test results at

this strain rate, a new sample geometry was designed aiming at:

- minimal plastic deformation at the transition between shoulders and gauge section or at the pin holes,
- uniaxial stress state in and around the centre of the gauge section before necking,
- total length smaller than 50 mm in order to be able to extract four samples along the length of the produced steel plates.

Finite Element (FE) simulations were used for the sample design. Next to the reference geometry, three other geometries were modelled. The R1 radius was enlarged to 2 and 3 mm for the R2 and R3 geometry, respectively. Additionally, a geometry was considered with a much smoother transition, following a clothoid curve with k-parameter 10, denoted as C geometry, see Fig. 8.

J2-plasticity was used to describe the material behaviour with a work hardening law based on the static behaviour of the Nb free steel. After all, the Nb free steel is characterised by the lowest strain hardening and is, therefore, most critical for the design of an optimal geometry (Fig. 7-a) [44].

The simulation results show that at the early stages of deformation, plastic deformation, indeed, starts in a limited region located at the transition to the gauge section or, in case of sample C, however at a lower extent, at the pins. Further deformation leads to onset of plastic deformation around the centre of the sample which subsequently
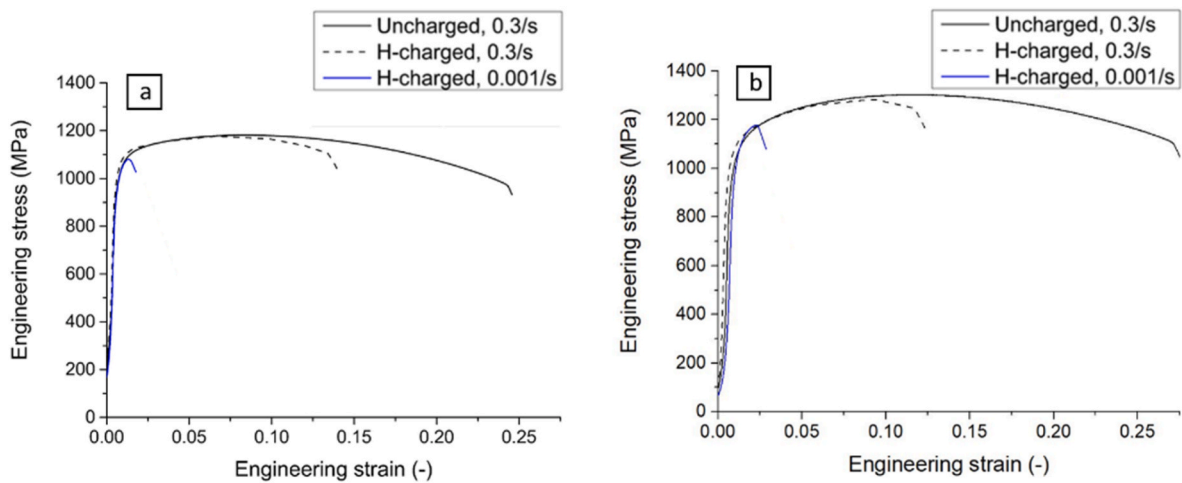
Fig. 7. Engineering tensile curves for (a) the Nb free and (b) the Nb steel tested in uncharged and H-charged conditions.
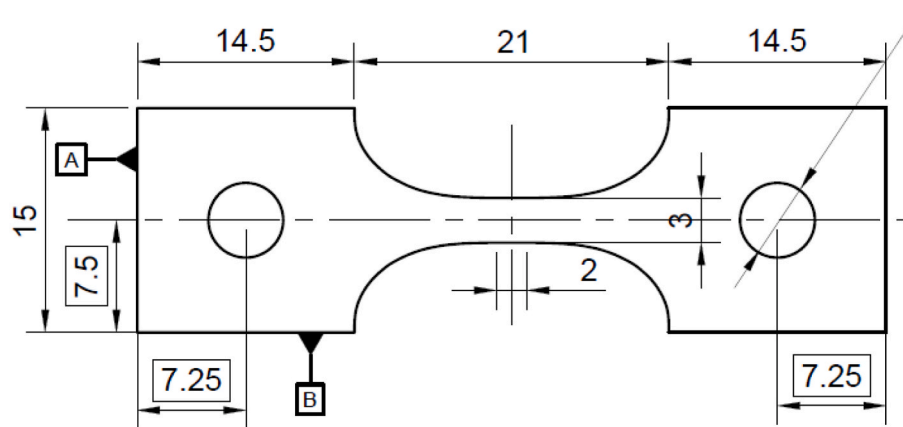

Fig. 8. Geometry C proposed for tensile tests at 0.001 s^{-1} strain rate with a transition zone following a clothoid curve.

increases and spreads towards the transition zones of the sample. From a certain moment on, the strain in the gauge section exceeds the strain in the transition zones or at the pins, and fracture is likely to occur in the gauge section. Therefore, to avoid failure outside the gauge section, the plastic deformation at this moment at the transition zones or pins should be as low as possible. In Fig. 9, plastic equivalent strain (PEEQ) distributions are represented in the R1, C and R3 samples at the transition moment. The displacement needed to obtain a higher plastic deformation in the gauge centre, together with the value of the highest PEEQ at the pins or transition zones are indicated. For the R1 geometry, a PEEQ value of 1.03% is observed in the transition zones. For the lowest strain rate static tensile tests, it can therefore be concluded that in the H-

charged samples the embrittlement was so severe that a plastic deformation of 1.03% could not be accommodated (Fig. 5). It is observed that with increasing the radius from 1 to 2 and further to 3 mm, the maximum PEEQ in the transition zone drops from 1.03% over 0.75%–0.36%. As far as the maximum PEEQ criterion is concerned, the clothoid geometry outperforms the other geometries: a PEEQ of only 0.12% at the pins has to be surpassed in order for the plastic deformation to be higher in the centre region of the tensile specimen.

Additionally, analysis of the non-axial stresses in the gauge section showed that, before necking, a uniaxial stress state can be assumed. Indeed, the highest non-axial stresses occur in the C sample, however, they are negligibly small: at an imposed strain of 5%, for example, the
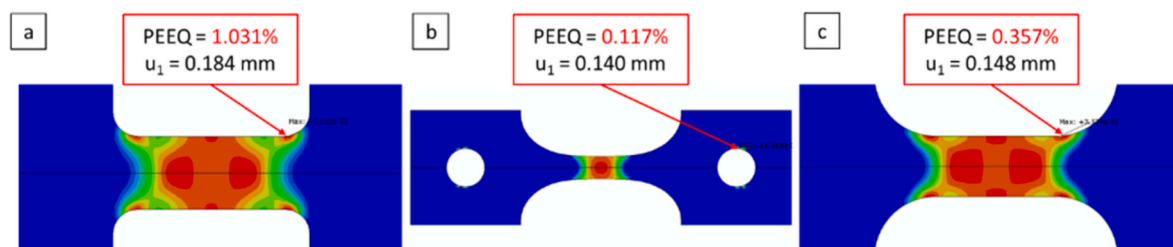
Fig. 9. Plastic equivalent strain distribution obtained by the FEM simulations for three different geometries: (a) R1, (b) C and (c) R3. The PEEQ strain at the shoulders and the pin connection for resp. the R1 and R3, and the clothoid geometry are shown just before the largest strain is observed along the gauge section of the specimen. The pin connection for the R1 and R3 samples is not shown as the strain in the transition zone is significantly larger than the strain observed at the pin connection and therefore of limited importance for the geometry design.

non-axial stress in the centre is below 0.9% of the axial stress.

For the reasons elaborated above, finally, geometry C was chosen to investigate the hydrogen embrittlement of the Q&P steels. From the simulations, a virtual gauge length was calculated and is found to be comparable to the gauge length of the R1 samples [45]. The use of the virtual gauge length was validated by comparing the uncharged test results obtained using both geometries. Quasi-identical curves were obtained [33]. To remove all possible uncertainty, all conclusions in the present work are, however, drawn based on the EI calculated using the same geometry for the charged and uncharged samples.

The tensile curves extracted at a strain rate of 0.001 s^{-1} and 0.03 s^{-1}, the latter of which is 10 times lower than what was possible for the R1 samples, of the Nb free and Nb samples, see Fig. 10, show that the presence of hydrogen again results in a significant decrease in the ductility of the Q&P steels. The 0.3s^{-1} strain rate tests were not repeated as the 0.03s^{-1} proved the success of the geometry [45]. At a strain rate of 0.03 s^{-1}, the EI is 44% and 57% for the Nb free and the Nb steel, respectively. The Q&P steel alloyed with Nb is more susceptible to hydrogen than the Nb free steel. Similar to the R1 samples tested at the highest static strain rate, i.e. at a strain rate of 0.03 s^{-1}, the fracture initiates in the centre of the gauge section.

For the samples tested at 0.001 s^{-1}, however, no EI is determined as the fracture was still not located in the gauge section, while in uncharged conditions the sample failed as expected inside the gauge zone (irrespective of the strain rate). Although at the moment of fracture, the FEM simulations predict that the highest strain occurs in the centre of the gauge section (cf. Fig. 9-b), the samples failed at locations between 3 and 5 mm away from the centre. The strain rate obtained from the FEM simulations for the C sample was calculated in the centre and at 3 and 5 mm away from the centre along the tensile axis [33]. It is noteworthy that at these fracture locations, because of the specific shape of the samples, the strain rate is 3–4 times smaller than in the centre. The locally reduced strain rate might have promoted HE.

The fracture surfaces of the Nb free and Nb Q&P steel are shown in Fig. 11 and 12, respectively, for charged (b-c) and uncharged samples (a) tested at a strain rate of 0.03 s^{-1}. For both steels, the fracture surfaces of the uncharged samples are covered with dimples, indicating a ductile fracture process characterised by void initiation, propagation and coalescence. Small differences can be observed between the fracture surfaces of the H-charged Nb free and Nb samples. Both steels show a fracture surface dominated by fish eyes and cleavage facets. In between the embrittled zones, small regions dominated by dimples are observed. However, the ductile bands are larger in the Nb free steel than in the Nb steel. Electron Dispersive X-ray Spectroscopy (EDX) analysis indicated the presence of CaS or Al-oxides in the center of these fish eyes, as

illustrated for the Nb steel in Fig. 13.

4.3.3. Dynamic tensile properties

The Q&P steels were tested at a strain rate of about 500s^{-1} using uncharged samples as well as hydrogen charged samples to evaluate the dynamic tensile properties. The results of the experiments are presented in Fig. 14. As opposed to the static tests, the presence of hydrogen only has a limited effect on the mechanical behaviour of both steels. The engineering tensile curves are similar, only a small reduction in the fracture strain is observed for the charged samples. The reduction in ductility is slightly more pronounced for the Nb free Q&P steel: an EI of 5.9% and 2.1% are obtained for the Nb free and the Nb steel, respectively. For all dynamic test samples, fracture initiated in the centre of the gauge section after clear necking.

SE micrographs of the fracture surfaces of H-charged samples are presented in Fig. 15. No differences are observed when comparing the Nb free (a) and the Nb steel (b). The surfaces of the charged samples are dominated by dimples and are hardly distinguishable from the uncharged reference samples tested at the same strain rate.

5. Discussion

5.1. Hydrogen characterisation

TDS curves are used to evaluate the hydrogen/microstructure interaction. Activation energies for different microstructural trapping sites (peak 1 and 2) are determined for both steels. It is observed that the peaks can be attributed to (i) dislocations and low angle grain boundaries (peak 1) and (ii) lath martensite (high angle) grain boundaries (Fig. 4) (peak 2) which are characterised by activation energies of about 22 kJ/mol and about 28 kJ/mol, respectively. This is in agreement with literature data [46,47]. The Nb steel is characterised by a small increases in activation energy which might be a result of neglecting re-trapping when using Kissinger's equation to determine the E_a and the influence of NbC. The larger trap density, as a result of the finer microstructure in the Nb steel, results in a higher potential for re-trapping [48]. Further, the activation energies of high angle martensite grain boundaries and NbC could be too similar to be distinguished as two separate peaks in this material [23,46]. The larger fraction of traps also explains the significant increase in the height of the second peak when compared to the Nb free steel.

The TDS measurements showed that the Nb steel contained an about 20% higher hydrogen content when charged under the same charging conditions as the Nb free steel. Hydrogen is known to diffuse to defects. These defects are, amongst others, grain boundaries, phase boundaries
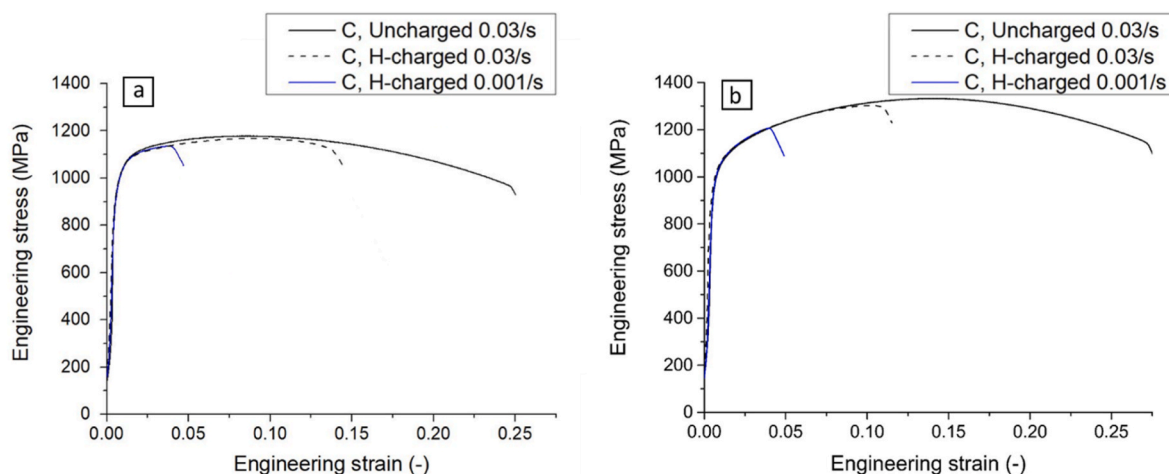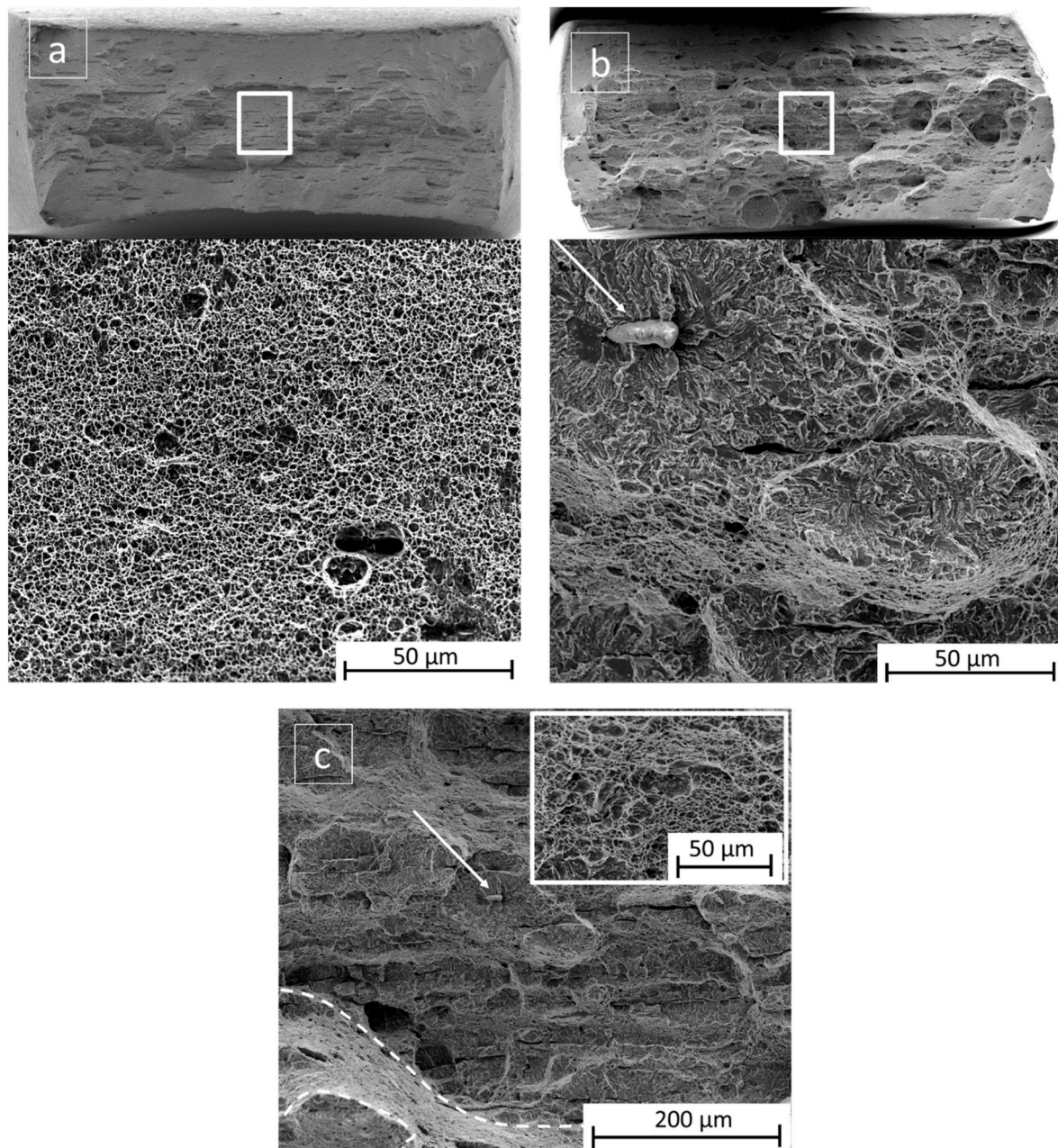

Fig. 10. Engineering tensile curves for the clothoid (C) geometry for (a) the Nb free and (b) the Nb steel tested under uncharged and H-charged condition at a strain rate of 0.001 s^{-1} and 0.03 s^{-1}.

Fig. 11. SE images of the fracture surfaces taken at the centre (indicated by a white square) of the Nb free steel tested at a strain rate of 0.03 s^{-1} for (a) uncharged and (b) H-charged samples. (c) gives an global view of the region surrounding the fish eye indicated by an arrow in (b). A band dominated by dimples is indicated by a dashed line of which an magnified view is presented in the insert.

and dislocations. Taking into account that the Nb steel is characterised by a 25% larger fraction of RA, as well as a smaller RA grain size, results in a significantly larger fraction of RA/martensite interface. Further, the martensite grains are about 35% finer in the Nb steel as well resulting mainly in an increase in high angle grain boundaries. On top of that, it is reported that the PAG boundaries need to be considered as hydrogen traps as well [49,50]. The Nb refinement effect on the PAG size will therefore have affected the measured hydrogen fraction. All differences between both materials indicate higher grain/phase boundaries in the Nb sample which can act as hydrogen traps resulting in the higher hydrogen uptake capacity. The higher number of boundaries is proven by the proportionally larger second peak, after deconvoluting the TDS curves, with respect to the first when comparing the Nb with the Nb free steel (Fig. 5). The second peak is attributed to martensite (high angle grain) boundaries. This is in agreement with the grain boundary density

analysis, as presented in Fig. 6, where the stable first peak corresponds to the low angle GB and the increase in the second peak can be attributed to high angle GB (Fig. 6). Secondly, in the Nb steel numerous, but fine, NbC are observed. The NbC are in literature often considered as weak to medium-strong hydrogen traps [23,27]. The trapping energy is proposed to be governed by the coherency of the interface which is determined by the size of the carbide [23,27]. In this work, NbCs with a size of about 10 nm are most likely to act as weak traps. The NbC might to a minor extent, although not decisively proven here, further increase the hydrogen content in the Nb steel. To summarise, it can be stated that the reason for the 25% larger hydrogen content in the Nb steel is mainly the result of the finer microstructure.
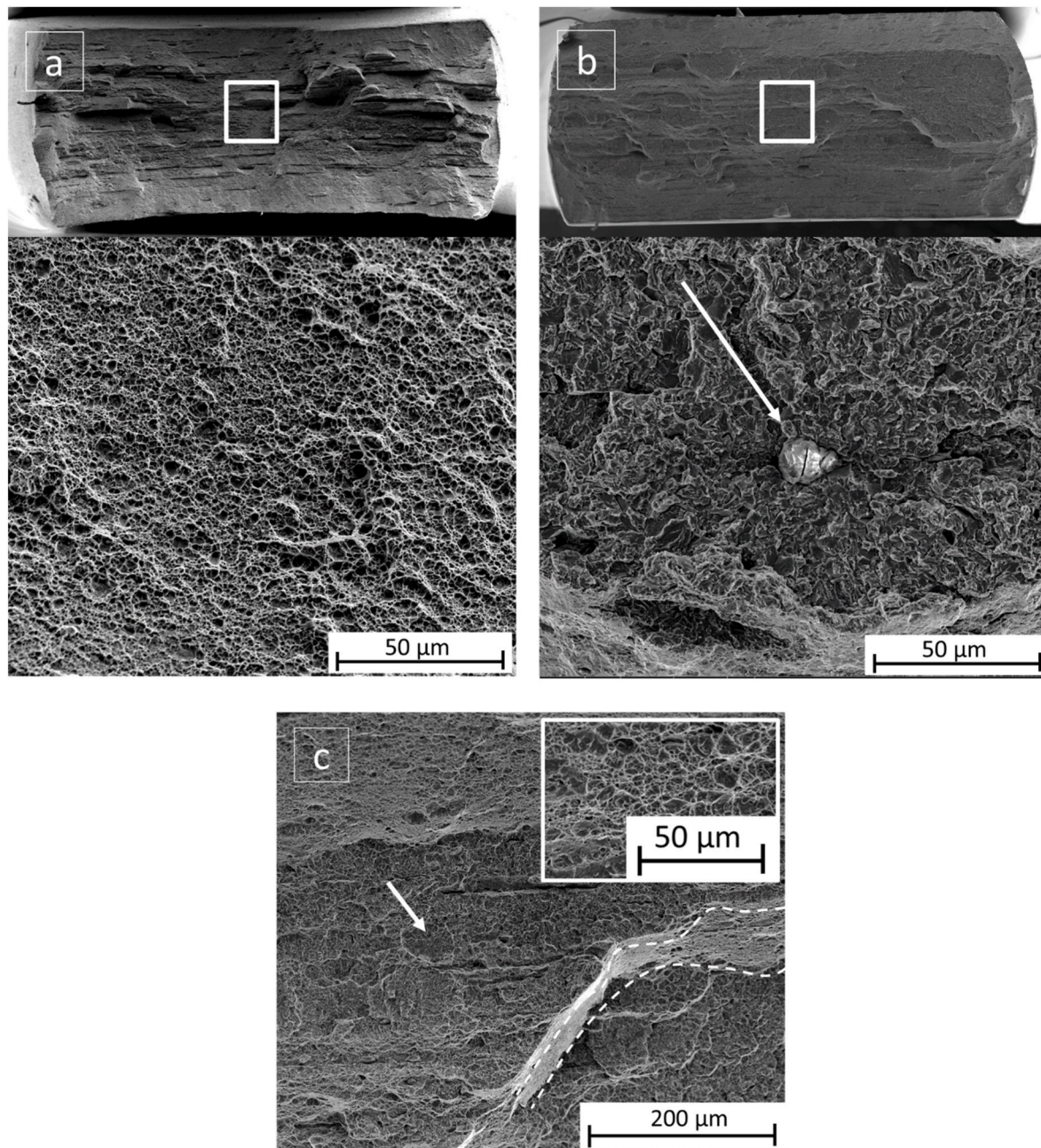
Fig. 12. SE images of the fracture surfaces taken at the centre (indicated by the white square) of the Nb steel tested at a strain rate of 0.03 s^{-1} for (a) uncharged and (b) H-charged samples. (c) gives an amplified view of the region surrounding the fish eye indicated by an arrow in (b). A band dominated by dimples is indicated by a dashed line of which a magnified view is presented in the insert.

5.2. Tensile properties

5.2.1. Static tensile properties

The presence of hydrogen resulted in a significant ductility reduction for both Q&P steels. A ductility reduction in TRIP-assisted steels is often attributed to decohesion of martensite/martensite interfaces via the hydrogen-enhanced interface decohesion (HEIDE) mechanism. Moreover, the hydrogen-enhanced localised plasticity (HELP) mechanism plays an important role in the propagation of cracks by affecting the dislocation movement [51]. The HEIDE phenomenon was first described in TRIP steels as the dominating mechanism for damage initiation while the HELP mechanism is dominating the crack propagation. Hydrogen affected the fracture mechanism, changing it from ductile to brittle as observed in the fracture surfaces examined via SEM. When comparing

the static tensile tests at a strain rate of 0.3 s^{-1} and 0.03 s^{-1}, the Nb free steel was less susceptible to hydrogen embrittlement than the Nb steel. The EI of the Nb steel was 28% higher than the Nb free steel which is attributed to the higher hydrogen content present in the Nb steel. For DP steel, it is reported that small increases in hydrogen content can significantly enlarge the HE [29]. Next to the total hydrogen content, the microstructural differences between both Q&P steels are also important in understanding the discrepancy in EI. A larger fraction of RA of low stability was present in the Nb steel. When transforming, RA is reported to be detrimental as martensite with a high carbon content is formed. This occurred in the region where hydrogen would be stored as it is expected that a thin layer of the austenite grains might be enriched with hydrogen or at least the martensite/austenite phase boundaries [13, 17–19]. The larger RA fraction with lower stability will result in a large
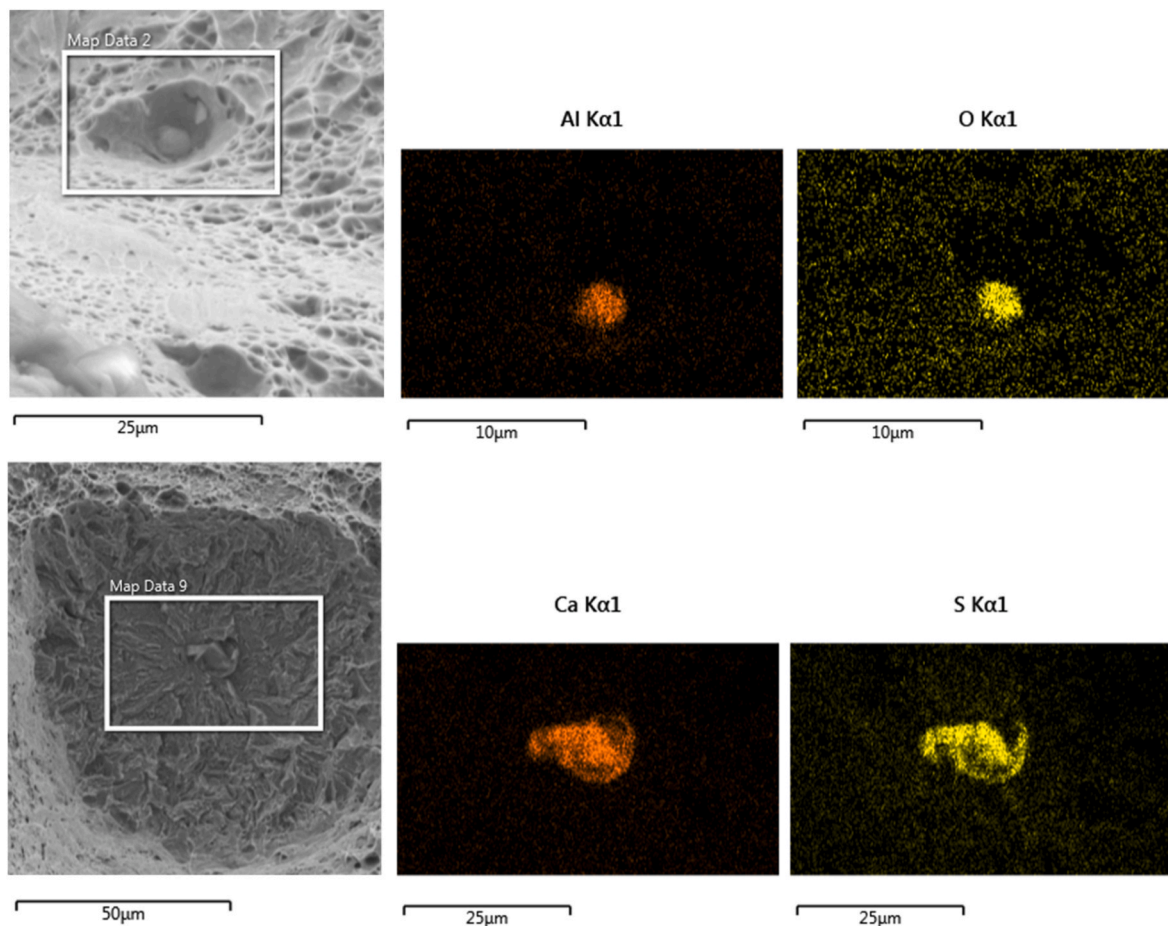
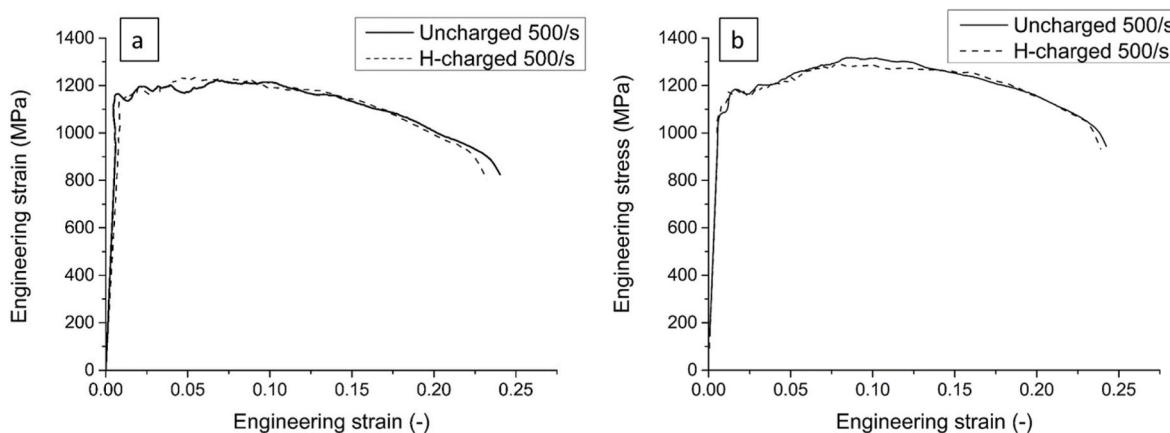**Fig. 13.** EDX measurements of the fisheye inclusions in the Nb steel.

Fig. 14. Engineering tensile curve for the dynamic tests carried out on (a) the Nb free as well as (b) the Nb steel. Curves show the behaviour of the uncharged as well as the H-charged steels.

fraction of potential hydrogen crack initiation points [52]. The higher susceptibility to hydrogen of the Nb steel is, therefore, attributed to the larger fraction of RA as well as to the higher hydrogen content. Comparing these results with samples tested at a 10 times higher speed, i.e. 0.3 s^{-1} (Fig. 10), it is observed that the EI slightly decreased at the increased strain rate, which is in agreement with studies on low carbon martensitic steels [53]. Hydrogen needs to diffuse to critical regions in order to embrittle the material at the macroscopic level by affecting the crack propagation (HELP). Increasing the strain rate reduces the time for diffusion which results in the decreased HE susceptibility.

The fracture surface of both steels was dominated by brittle regions. These zones often formed around brittle precipitates or inclusions and were characterised by cleavage facets, as indicated by the arrow in Fig. 11 [29]. Both were characterised by the presence of Mn-sulfides/Al-oxides based "fish eyes". However, the fracture surfaces of the Nb free and the Nb steel showed some differences. Although fish eyes were observed in both steels, ductile zones in between the brittle regions existed. Indeed, bands with clear dimples were present in the fracture surfaces. However, the ductile regions were smaller in the Nb steel in line with the observations on the EI values of both steels. The, on
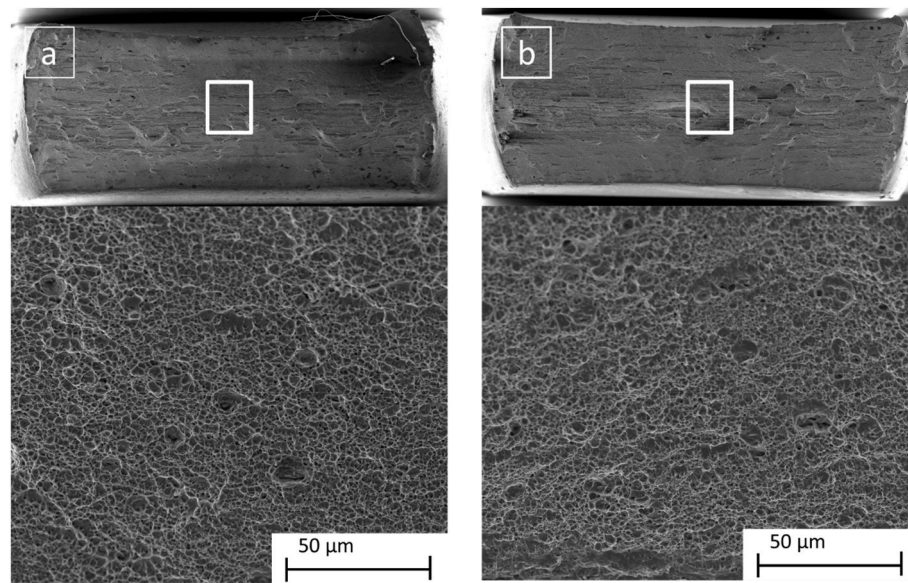
Fig. 15. SE images of the fracture surfaces taken at the centre (indicated by a white square) on the hydrogen charged samples tested under dynamic conditions. The images presented are of (a) the Nb free steel and (b) the Nb steel.

average, smaller ductile fracture zones in the Nb steel is in agreement with literature [53].

The use of a sample with smoother transition regions, i.e. the C sample, allowed the strain rate to be reduced by a factor of 10 to 0.03 s⁻¹. However, it was observed that samples tested at an even lower speed of 0.001 s⁻¹, independent of the geometry used, failed outside the gauge section. At the moment and location of failure, the strain, and thus also strain rate, was significantly lower than the value in the gauge section. Since, the tests showed that reducing the strain rate significantly increased the HE, it is believed that this lower strain rate led to fracture.

5.2.2. Dynamic tensile properties

The hydrogen embrittlement susceptibility under dynamic conditions was rather limited. An EI of 5.9% and 2.1% was observed for the Nb free and the Nb steel, respectively. These EIs are significantly lower compared to the static test values (Table 6). The effect of the strain rate on the HE is attributed to several factors. Firstly, it is reported that during high strain rate experiments, the TRIP effect is suppressed as a result of the adiabatic temperature increase (>80 °C) of the material [28]. Because of the smaller fraction of untempered martensite formed in the dynamic tests, the role of hydrogen on the ductility of the Q&P steels is limited, which confirms the importance of the RA stability, as reported in literature [21]. Secondly, and more importantly, the reduced diffusion of hydrogen, due to the inherent short duration of dynamic tests, further contributed to the low EI values. The short testing times caused the diffusion of hydrogen to be severely limited. For a DP steel, it was also reported that the embrittlement of the steel in the presence of hydrogen was significantly smaller in dynamic tests compared to static tests [29]. This was fully attributed to the limited diffusion distance of hydrogen during the dynamic tests, i.e. reported to be ≈ 0.2 μm at a strain rate similar to the one in the present study [29]. During the static tensile tests, hydrogen creates an atmosphere around dislocations, enhancing (HELP mechanism) their mobility which results in faster crack propagation. However, during the dynamic experiments, the

hydrogen atoms cannot affect the dislocation mobility to the same extent and their effect on the ductility is minor. In correspondence with the limited HE, the fracture surface of the dynamically tested samples was dominated by dimples characteristic for a ductile fracture mode.

Although the HE of Q&P steels is rather limited at high strain rates, still a difference was seen when comparing the Nb free steel with the Nb steel. While the addition of Nb increased the hydrogen susceptibility when tested under static conditions, an opposite trend was detected when tested at high strain rates. An explanation could be found in the larger post-necking behavior of the Nb free steel (cf. Fig. 14) where ductile fracture can be accelerated through the influence of hydrogen on dislocations (HELP) and the nucleation and stabilization of vacancies (HESIV) [54,55].

6. Conclusions

The effect of the addition of Nb on the hydrogen embrittlement susceptibility of a Q&P steel was investigated under static and dynamic test conditions. The mechanical test results were linked with the microstructural features of the steels. For this purpose, the effect of Nb on the grain size, phase fraction and stability of the retained austenite were discussed. The main conclusions of the study are summarised hereafter:

- The addition of Nb results in a higher hydrogen uptake due to the refined martensite matrix, the NbC precipitates and the larger fraction of small RA grains.
- The desorption of hydrogen, determined via TDS measurements, is shifted to higher temperatures due to more retrapping of hydrogen when Nb is added. More retrapping, giving rise to slow hydrogen desorption characteristics, was attributed to the more refined structure and the presence of Nb carbides.
- The higher hydrogen content, as well as the larger fraction of low stability RA in the Nb steel, resulted in an increased hydrogen embrittlement susceptibility in the Nb steel compared to the Nb free steel when tested under static conditions.
- Adapting the dog-bone tensile sample using a smoother clothoid based transition from the clamping zone to the gauge section, to remove the strain concentration at the shoulder section prior to localization in the centre of the gauge section, was needed to obtain reliable low strain rate test results for the H-charged samples.

Table 6
Embrittlement index as a function of the strain rate for both steels.

	0.03 s⁻¹	0.3 s⁻¹	500 s⁻¹
Nb free steel	44.9% ± 1.1	40.8% ± 1.5	5.9% ± 1.5
Nb steel	57.4% ± 2.2	52.0% ± 1.5	2.1% ± 1.5

- Imposing high strain rates reduced the hydrogen embrittlement in both steels. Dynamic strain rates even almost completely suppressed the negative effect of hydrogen on the ductility. This was explained by the reduction in the hydrogen diffusion distance and the suppression of the TRIP effect due to adiabatic heating of the steel during dynamic testing.
- At dynamic strain rates, the Nb steel showed an improved hydrogen resistance compared to the Nb free steel.

CRediT authorship contribution statement

Florian Vercruysse: Conceptualization, Investigation, Formal analysis, Writing – original draft. **Lisa Claeys:** Conceptualization, Investigation, Formal analysis, Writing – review & editing. **Tom Depover:** Conceptualization, Funding acquisition, Writing – review & editing. **Patricia Verleysen:** Funding acquisition, Writing – review & editing. **Roumen H. Petrov:** Funding acquisition, Writing – review & editing. **Kim Verbeken:** Funding acquisition, Writing – review & editing.

Declaration of competing interest

The authors declare that they have no known competing financial interests or personal relationships that could have appeared to influence the work reported in this paper.

Data availability

The data that has been used is confidential.

Acknowledgement

References

[1] M. Gouné, F. Danoix, S. Allain, O. Bouaziz, Unambiguous carbon partitioning from martensite to austenite in Fe-C-Ni alloys during quenching and partitioning, Scripta Mater. 68 (12) (2013) 1004–1007.

[2] D.K. Matlock, J.G. Speer, E. De Moor, P.J. Gibbs, Recent developments in advanced high strength sheet steels for automotive applications: an overview, Eng. Sci. Technol. an Int. J. 15 (1) (2012) 1–12.

[3] J. Speer, D.K. Matlock, B.C. De Cooman, J.G. Schroth, Carbon partitioning into austenite after martensite transformation, Acta Mater. 51 (9) (2003) 2611–2622.

[4] T.D. Bigg, D.V. Edmonds, E.S. Eardley, Real-time structural analysis of quenching and partitioning (Q&P) in an experimental martensitic steel, J. Alloys Compd. 577 (2013) S695–S698.

[5] J.G. Speer, E. De Moor, A.J. Clarke, Critical assessment: quenching and partitioning, Mater. Sci. Technol. 31 (1) (2015) 3–9.

[6] D.V. Edmonds, K. He, F.C. Rizzo, B.C. De Cooman, D.K. Matlock, J.G. Speer, Quenching and partitioning martensite-A novel steel heat treatment, Mater. Sci. Eng. A 438 (440) (2006) 25–34.

[7] A. Grajcar, R. Kuziak, W. Zalecki, Third generation of AHSS with increased fraction of retained austenite for the automotive industry, Arch. Civ. Mech. Eng. 12 (3) (2012) 334–341.

[8] J. Mola, B.C. De Cooman, Quenching and partitioning (Q&P) processing of martensitic stainless steels, Metall. Mater. Trans. A Phys. Metall. Mater. Sci. 44 (2) (2013) 946–967.

[9] T.B. Hilditch, S.B. Lee, J.G. Speer, D.K. Matlock, Response to Hydrogen Charging in High Strength Automotive Sheet Steel Products, SAE Technical Paper, 2003.

[10] G. Lovicu, et al., Hydrogen embrittlement of automotive advanced high-strength steels, Metall. Mater. Trans. A Phys. Metall. Mater. Sci. 43 (11) (2012) 4075–4087.

[11] J.A. Ronevich, J.G. Speer, D.K. Matlock, Hydrogen embrittlement of commercially produced advanced high strength sheet steels, SAE Int. J. Mater. Manuf. 3 (1) (2010) 255–267.

[12] T. Michler, J. Naumann, Microstructural aspects upon hydrogen environment embrittlement of various bcc steels, Int. J. Hydrogen Energy 35 (2) (2010) 821–832.

[13] X. Zhu, W. Li, H. Zhao, L. Wang, X. Jin, Hydrogen trapping sites and hydrogen-induced cracking in high strength quenching & partitioning (Q&P) treated steel, Int. J. Hydrogen Energy 39 (24) (2014) 13031–13040.

[14] M. Enomoto, D. Hirakami, T. Tarui, Thermal desorption analysis of hydrogen in high strength martensitic steels, Metall. Mater. Trans. A Phys. Metall. Mater. Sci. 43 (2) (2012) 572–581.

[15] T. Depover, D. Wan, D. Wang, A. Barnoush, K. Verbeken, The effect of hydrogen on the crack initiation site of TRIP-assisted steels during in-situ hydrogen plasma micro-tensile testing: leading to an improved ductility? Mater. Char. 167 (July) (2020), 110493.

[16] R.O. Ritchie, M.H.C. Cedeno, V.F. Zackay, E.R. Parker, Effects of silicon additions and retained austenite on stress corrosion cracking in ultrahigh strength steels, Metall. Trans. A 9 (1) (1978) 35–40.

[17] C. Andreone, A. Murut, Influence of the austenite retained in the hydrogen embrittlement in AISI 4340, Scripta Metall. Mater. 24 (8) (1990) 1453–1458.

[18] F. Solana, C. Takamadate, I.M. Bernstein, W. Thompson, The role of retained austenite in stress corrosion cracking of steels, Metall. Trans. A 18 (6) (1991) 1023–1028.

[19] Y.-H. Kim, H.J. Kim, J.W. Morris, The influence of precipitated austenite on hydrogen embrittlement in 5.5 Ni steel, Metall. Trans. A 17 (7) (1986) 1157–1164.

[20] X. Zhu, K. Zhang, W. Li, X. Jin, Effect of retained austenite stability and morphology on the hydrogen embrittlement susceptibility in quenching and partitioning treated steels, Mater. Sci. Eng. A 658 (2016) 400–408.

[21] J. Yang, F. Huang, Z. Guo, Y. Rong, N. Chen, Effect of retained austenite on the hydrogen embrittlement of a medium carbon quenching and partitioning steel with refined microstructure, Mater. Sci. Eng. A 665 (2016) 76–85.

[22] Y. Du, et al., Hydrogen embrittlement behavior of high strength low carbon medium manganese steel under different heat treatments, Int. J. Hydrogen Energy 44 (60) (2019) 32292–32306.

[23] M. Ohnuma, J. ichi Suzuki, F.G. Wei, K. Tsuzaki, Direct observation of hydrogen trapped by NbC in steel using small-angle neutron scattering, Scripta Mater. 58 (2) (2008) 142–145.

[24] H.G. Lee, J.Y. Lee, Hydrogen trapping by TiC particles in iron, Perspect Hydrog. Met 32 (1) (1986) 421–426.

[25] P. Xu, C. Li, W. Li, M. Zhu, K. Zhang, Effect of microstructure on hydrogen embrittlement susceptibility in quenching-partitioning-tempering steel, Mater. Sci. Eng. A 831 (Jan. 2022), 142046.

[26] S. Zhang, et al., Dual role of nanosized NbC precipitates in hydrogen embrittlement susceptibility of lath martensite steel, Corrosion Sci. 164 (2020) 108345.

[27] E. Wallaert, T. Depover, M. Arafin, K. Verbeken, Thermal desorption spectroscopy evaluation of the hydrogen-trapping capacity of NbC and NbN precipitates, Metall. Mater. Trans. A Phys. Metall. Mater. Sci. 45 (5) (2014) 2412–2420.

[28] F. Vercruysse, C. Celada-casero, B.M. Linke, P. Verleysen, R.H. Petrov, Temperature dependence of the static and dynamic behaviour in a Quenching and Partitioning processed low Si steel, Metals (Basel) 10 (4) (2020) 509.

[29] T. Depover, F. Vercruysse, A. Elmahdy, P. Verleysen, K. Verbeken, Evaluation of the hydrogen embrittlement susceptibility in DP steel under static and dynamic tensile conditions, Int. J. Impact Eng. 123 (2019).

[30] A. Smith, F. Vercruysse, R. Petrov, P. Verleysen, The effect of Niobium on austenite evolution during hot rolling of advanced high strength steel, J. Phys. Conf. seres 1270 (1) (2019).

[31] D.P. Koistinen, R.E. Marburger, A general equation prescribing the extent of the austenite-martensite transformation in pure iron-carbon alloys and plain carbon steels, Acta Metall. 7 (1959) 59–60.

[32] C. Capdevila, F.G. Caballero, C. García De Andrés, Determination of Ms temperature in steels: a Bayesian neural network model, ISIJ Int. 42 (8) (2002) 894–902.

[33] F. Vercruysse, Microstructure-Properties Control of Third Generation Advanced High Strength Steels via Ultrafast Annealing and Quenching and Partitioning, Ghent University, 2021.

[34] R.H. Petrov, L.A.I. Kestens, Advanced High-Strength Steels: Electron Backscatter Diffraction (EBSD), CRC Press, 2016.

[35] M.J. Santofimia, R.H. Petrov, L. Zhao, J. Sietsma, Microstructural analysis of martensite constituents in quenching and partitioning steels, Mater. Char. 92 (2014) 91–95.

[36] B.D. Cullity, Elements of X-Ray Diffraction, Addison-Wesley Publishing, Inc., New Jersey, 1956.

[37] M.J. Santofimia, T. Nguyen-Minh, L. Zhao, R. Petrov, I. Sabirov, J. Sietsma, New low carbon Q&P steels containing film-like intercritical ferrite, Mater. Sci. Eng. A 527 (21) (2010) 6429–6439.

[38] N.H. Van Dijk, et al., Thermal stability of retained austenite in TRIP steels studied by synchrotron X-ray diffraction during cooling, Acta Mater. 53 (20) (2005) 5439–5447.

[39] H.E. Kissinger, Reaction kinetics in differential thermal analysis, Anal. Chem. 29 (11) (1957) 1702–1706.

[40] M.A. Meyers, Dynamic Behavior of Materials, John Wiley & Sons, Inc, Hoboken, NJ, USA, 1994.

[41] P. Verleysen, J. Degrieck, T. Verstraete, J. Van Slycken, Influence of specimen geometry on split Hopkinson tensile bar tests on sheet materials, Exp. Mech. 48 (5) (Oct. 2008) 587–598.

[42] R. Zaera, J.A. Rodríguez-Martínez, D. Rittel, On the Taylor–Quinney coefficient in dynamically phase transforming materials. Application to 304 stainless steel, Int. J. Plast. 40 (2013) 185–201.

[43] C. Cayron, ARPGE : a computer program to automatically reconstruct the parent grains from electron backscatter diffraction data, J. Appl. Crystallogr. 40 (6) (2007) 1183–1188.

[44] F. Vercruysse, C. Celada-Casero, B.M. Linke, P. Verleysen, R.H. Petrov, The effect of Nb on the strain rate and temperature dependent behaviour of quenching & partitioning steels, Mater. Sci. Eng. A 800 (July 2020) (2021), 140293.

[45] P. Verleysen, J. Degrieck, Experimental investigation of the deformation of Hopkinson bar specimens, Int. J. Impact Eng. 30 (3) (2004) 239–253.

[46] R.L.S. Thomas, D. Li, R.P. Gangloff, J.R. Scully, Trap-governed hydrogen diffusivity and uptake capacity in ultrahigh-strength AERMET 100 steel, Metall. Mater. Trans. A Phys. Metall. Mater. Sci. 33 (7) (2002) 1991–2004.

[47] F.G. Wei, T. Hara, K. Tsuzaki, Precise determination of the activation energy for desorption of hydrogen in two Ti-added steels by a single thermal-desorption spectrum, Metall. Mater. Trans. B Process Metall. Mater. Process. Sci. 35 (3) (2004) 587–597.

[48] R. Kirchheim, Bulk diffusion-controlled thermal desorption spectroscopy with examples for hydrogen in iron, Metall. Mater. Trans. A Phys. Metall. Mater. Sci. 47 (2) (2016) 672–696.

[49] A. Shibata, T. Murata, H. Takahashi, T. Matsuoka, N. Tsuji, Characterization of hydrogen-related fracture behavior in as-quenched low-carbon martensitic steel and tempered medium-carbon martensitic steel, Metall. Mater. Trans. A Phys. Metall. Mater. Sci. 46 (12) (2015) 5685–5696.

[50] A. Shibata, H. Takahashi, N. Tsuji, Microstructural and crystallographic features of hydrogenrelated crack propagation in low carbon martensitic steel, ISIJ Int. 52 (2) (2012) 208–212.

[51] A. Laureys, T. Depover, R. Petrov, K. Verbeken, Characterization of hydrogen induced cracking in TRIP-assisted steels, Int. J. Hydrogen Energy 40 (47) (2015) 16901–16912.

[52] A. Laureys, T. Depover, R. Petrov, K. Verbeken, Microstructural characterization of hydrogen induced cracking in TRIP-assisted steel by EBSD, Mater. Char. 112 (2016) 169–179.

[53] Y. Momotani, A. Shibata, D. Terada, N. Tsuji, Effect of strain rate on hydrogen embrittlement in low-carbon martensitic steel, Int. J. Hydrogen Energy 42 (5) (2017) 3371–3379.

[54] M. Nagumo, Hydrogen related failure of steels - a new aspect, Mater. Sci. Technol. 20 (8) (2004) 940–950.

[55] M. Nagumo, K. Takai, The predominant role of strain-induced vacancies in hydrogen embrittlement of steels: Overview, Acta Mater. 165 (2019) 722–733.